Fabrication of mesoporous crystalline microparticles of poly(ether sulfone) via solvent-induced crystallization

Sadaki Samitsu[*]

National Institute for Materials Science (NIMS), 1-2-1, Sengen, Tsukuba, Ibaraki 305-0047, Japan

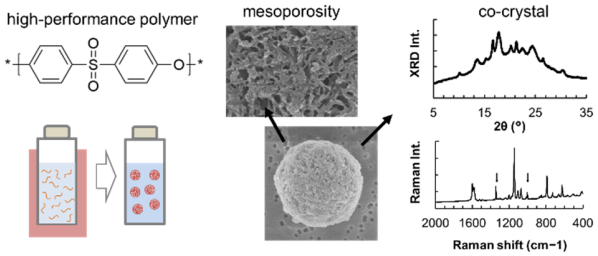

for Table of Contents use only

ABSTRACT

Mesoporous polymer microparticles are promising for energy, environmental, and biomedical applications. A linear polymer microparticle is desirable from the perspective of polymer

recycling. In this study, mesoporous crystalline microparticles of a commercially available high-performance polymer, poly(ether sulfone) (PES), were prepared. Solvent-induced crystallization of PES in nitrobenzene resulted in nearly spherical microparticles with an average size of 5 μm and narrow size distribution. The microstructure and mesoporosity of the microparticles were characterized with scanning electron microscopy, X-ray diffraction, differential scanning calorimetry, and nitrogen adsorption/desorption, which gave a pore size distribution peaking at 7 nm with a porosity of 0.44. Fourier-transform infrared spectroscopy, Raman spectroscopy, and thermogravimetric analysis confirmed the cocrystal of PES and nitrobenzene. The formation mechanism of the PES microparticles was elucidated based on the theory of polymer spherulite formation. This study gives an insight on solvent-induced crystallization of rigid high-T_g polymers useful for the mesoporous polymer particle fabrication.

INTRODUCTION

Mesoporous polymer particles have interesting properties and are promising materials for applications such as battery polyelectrolytes [1,2], healthcare and pharmaceuticals [3,4,] supports for catalysts and nanoparticles [5,6,] and optics [7]. Therefore, the fabrication of mesoporous particles is intriguing and has been extensively investigated so far [8–10].. The most popular fabrication method is suspension polymerization and its derived methods, in which an optimal choice of porogen and polymerization conditions provide particles of different sizes, shapes, and pore structures in a controlled manner [11,12]. Despite several advantages, however, polymer crosslinking is usually required to maintain the mesoporosity [13], which severely impacts the reprocessing and does not meet the recent norms for polymer recycling. Therefore, the fabrication of mesoporous particles from a linear polymer is a major challenge in polymer science. The mesopore stability of

polymers can be increased by crystallization and high rigidity of the polymer main chain. Thus, mesoporous particle fabrication via crystallization of a high-performance polymer in a solution is a promising approach that has not yet been reported. Thermally induced and solvent-induced deformation of mesoporous microparticles may also provide additional possibilities for stimuli-response applications.

Polymer crystallization in a solution is used as a physical principle of membrane fabrication, which is well-known as thermally induced phase separation or solid-liquid phase separation [14,15]. Compared to membrane fabrication focusing on the interconnected morphology of polymer self-assembly, crystallization-mediated particle fabrication has not been established because it requires another approach for isolating polymer self-assembly at the microscale. Several groups have reported the formation of spherical particles by crystallizing poly(ethylene oxide) [16,17], isotactic polystyrene [18], poly(L-lactide) [19], and polyamide 6 (nylon 6) [20,21]. Unfortunately, however, most of these studies did not investigate the mesoporous structure of the particles in detail. It is argued that the flexible polymers forming the particles are inadequate for sustaining mesoporosity. Therefore, a polymer with a rigid backbone is desirable for the formation of mesoporous crystalline structures despite the rarity of crystallization in rigid polymers. Daniel et al. reported solvent-induced crystallization of rigid polymers syndiotactic polystyrene and poly(2,6-dimethyl-1,4-phenylene oxide) to successfully form nanoporous structures that were stable in the dried state [22-23]. Solvent-induced crystallization is a process in which polymers crystallize with the assistance of solvent molecules. Sometimes semicrystalline and even amorphous polymers in the bulk state are crystallized in a solution because of the formation of cocrystals with solvent molecules and/or the plasticization effect of the solvent. Crystallization of semicrystalline poly(ethylene terephthalate) and amorphous poly(carbonate) was discovered

in the 1960s [24], and it has been investigated in isotactic poly(propylene) [25], syndiotactic poly(styrene) [26,27], poly(2,6-dimethyl-1,4-phenylene)oxide [28], and poly(lactic acid) [29] to form cocrystals with solvent molecules. Guenet summarized such crystallization behavior of synthetic polymers and biopolymers as the part of the polymer-solvent molecular compounds [30]. The solvent-induced crystallization was also found on high-performance polymers that have a high glass transition temperature (T_g) above 200 °C and are classified as an amorphous polymer in bulk. Blackadder et al. reported poly(ether sulfone) (PES) crystallized in dichloromethane,[31,32] of which crystal structure Benhalima et al. investigated by X-ray diffraction using a low-molecular-weight model compound.[33] Recently, Handge and coworkers reported the solvent-induced crystallization of poly(phenyl sulfone) to form cocrystals with *N*,*N*-dimethyl formamide (DMF) and *N*,*N*-dimethyl acetamide [34]. In a previous study by the author, solvent-induced crystallization of another high-performance polymer, poly(ether sulfone) (PES), in a DMF-benzene mixture was reported [35]. The percolation network growth of PES nanofibrils caused physical gelation of the solution, which enabled the facile fabrication of a mesoporous PES monolith. The mesoporous monolith had high thermal stability of the mesopores (up to 150 °C) due to the high T_g of PES. In this study, owing to successive and comprehensive solvent exploration, solvent-induced crystallization of PES in a single solvent system (nitrobenzene) was found, which allowed the systematic investigation of the crystallization behavior of PES. Interestingly, crystallization afforded nearly spherical mesoporous microparticles. From the perspective of potential application, fabrication of macroscopic material shapes such as films, monoliths, and particles is important because the shapes determine the usage of the materials. Most studies on porous polymer fabrications via polymer crystallization in solutions have reported that aerogel monoliths via physical gelation and particle formation via spherulite formation are limited.

Considering the author's previous work [35], this study demonstrated that the same polymer, PES, gives different macroscopic morphologies in solvent-induced crystallization and suggests the possibility of targeting self-assembly of homopolymers using solution crystallization. The crystalline structure was validated using X-ray diffraction (XRD) and differential scanning calorimetry (DSC). Nitrobenzene molecules trapped in the cocrystals were detected using Fourier-transform infrared (FT-IR) and Raman spectroscopies as well as thermogravimetric analysis (TGA), which confirmed the room-temperature stability of the cocrystals when subjected to vacuum drying. The formation mechanism of the microparticles was elucidated based on the growth of the polymer spherulites.

EXPERIMENTAL

Chemicals

PES powder (SUMIKAEXCEL 3600P) was supplied by Sumitomo Chemical (Japan). The number average and weight average molecular weights (M_n and M_w) of the PES are 28000 and 47000, respectively, which were analyzed using gel permeation chromatography (GPC). All organic solvents (purity, ≥95%) (Supporting Information) were purchased from Tokyo Chemical Industry (Japan). The boiling temperature (T_b) and melting temperature (T_m) of the solvents were referred from a solvents handbook [36] and are listed in Table S1 (Supporting Information).

Preparation of PES microparticles

In a typical procedure (Scheme 1), PES powder (2.0 g) was added to nitrobenzene (8.0 g) under stirring at room temperature (25 ± 2 °C, unless otherwise stated) for 10 min and heated at 140 °C for 0.5 h for complete dissolution. The 20 wt.% solution was cooled to room temperature under

vigorous magnetic stirring. The clear solution gradually became turbid at room temperature while under stirring. The time course of the appearance change depends on the PES concentration, as discussed later. The white solution was poured into an excess amount of methanol (5–10 times the weight of nitrobenzene), and solid microparticles were collected via centrifugation (3000 rpm, 3 min). The microparticles were sequentially washed with methanol (2 times), ethanol (1 time), and hexane (2 times). After the solvent exchange, the particles were vacuum-dried at room temperature for at least 24 h using a rotary pump (GCD-136X, ULVAC KIKO, Japan). The process yielded fine microparticles in a dried state with high yields (≥90%). The microparticles are denoted by the PES concentration (C_p) of the solution; for example, P20 indicates PES microparticles obtained from a 20 wt.% solution.

Scheme 1. (a) Chemical structure of PES. (b) Preparation procedure of PES microparticles.

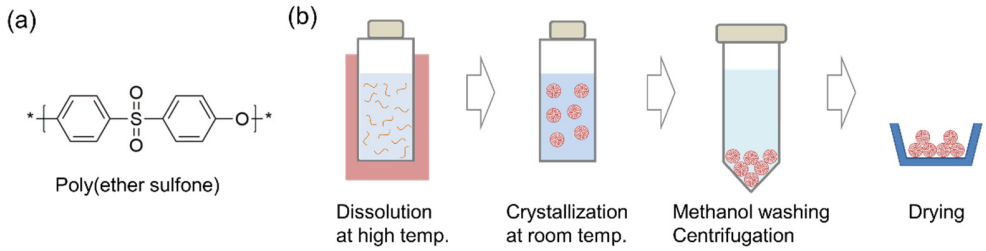

Characterization of PES microparticles

The particle size distribution was measured using a laser diffraction particle size analyzer (SALD-2100, Shimadzu, Japan). PES microparticles were dispersed in methanol by 15-min ultrasonication before the measurements. The particle size was analyzed assuming a spherical particle shape and the complex refractive index of a PES particle to be 1.60−0.10i. Shape and surface morphology of the microparticles were observed using scanning electron microscopy (SEM) (S-4800, Hitachi, Japan) at an acceleration voltage of 5 kV. The microparticles were dispersed in methanol via ultrasonication, filtered using a track-etched polycarbonate membrane

(Isopore, pore size: 0.22 μm, Millipore) , and coated with a platinum layer via ion sputtering (E-1030, Hitachi, Japan). The specific surface area (S_{BET}), meso, macro, and total pore volumes (V_{meso}, V_{macro}, V_{total}) were evaluated using a gas adsorption analyzer (BELSORP-MAX, MicrotracBEL, Japan). X-ray diffraction (XRD) patterns were recorded using a benchtop X-ray diffractometer (MiniFlex 600, Rigaku, Japan). A wet sample was obtained as an intermediate product by directly filtering the microparticles from the 20-wt.% solution without methanol washing. Fourier transform infrared (FT-IR) spectroscopy (IRTracer-100, Shimadzu, Japan) analyses were performed using a single reflection diamond crystal attenuated total reflectance accessory (Quest, Specac). Raman spectroscopy (RAMANplus, Nanophoton, Japan) was performed with a 785-nm excitation laser to avoid the fluorescence emission of PES. Owing to the limited spectral window of the detector, Raman spectra were recorded at a few separate ranges under the same measurement conditions and merged into one by adding a small spectrum offset. The thermal behavior of the microparticles was studied using differential scanning calorimetry (DSC) (Q2000, TA instruments, USA). Nitrogen gas (flow rate = 50 mL/min) was used as the carrier gas. TGA was performed using an STA/TG-DSC instrument (STA 2500 Regulus, NETZSCH, Germany) in the temperature range of 25–300 °C (heating rate: 5 °C/min) under a nitrogen flow of 20 mL/min. The microparticles (5–10 mg) were vacuum-dried at room temperature prior to the analysis.

Characterization of PES solution

Prior to the experiments, the dissolution behavior of PES in various organic solvents was preliminarily examined based on the Hansen solubility parameter (HSP) calculated using a commercial software (HSPiP, ver. 5.2). In the general case of polymer crystallization in a solution, a polymer dissolves in an organic solvent at a high temperature and crystallizes at a low

temperature due to supersaturation caused by the temperature drop. The maximum and minimum experimentally-accessible operation temperatures are constrained by the T_b and T_m of a good solvent, respectively. To ensure a large supersaturation by cooling to room temperature, solvents with a high T_b (≥ 100 °C) and low T_m (≤ 20 °C) were selected from the list of organic solvents provided in the software. The HSP values of the solvents and their relative energy difference (RED) to PES are listed in Table S1. The RED value is an indicator of polymer dissolution, suggesting that a solvent will dissolve (RED < 1), partially dissolve (RED = 1), and not dissolve (RED > 1) a polymer [37]. Accordingly, PES dissolution in 21 organic solvents was tested with a C_p of 10 wt.% at 140 °C. Solvents with T_b < 140 °C were tested at 100 °C. Solutions with completely dissolved PES at high temperatures were tested for phase separation at room temperature. The phase separation behavior was visually inspected for turbidity at room temperature after a few days.

Gel permeation chromatography (GPC) was performed with JASCO EXTREMA system equipped with polystyrene mixed gel columns at 40 °C using RI detector and DMF as an eluent. The GPC was calibrated with PMMA standards. The optical transmittance of the PES solutions was monitored at a wavelength of 500 nm using an Ultraviolet-visible spectrometer (V-670, JASCO, Japan) equipped with a Peltier temperature control unit. The PES solution prepared at 140 °C was sealed in a quartz cell with a 10-mm cell length. The solution was equilibrated at 100 °C for 5 min and quenched at the targeted crystallization temperature for isothermal crystallization.

Details of the XRD measurements, gas adsorption experiments, and PES solubility examined using HSP have been reported previously by the author [35].

RESULTS AND DISCUSSION

Thermal behavior of PES solution

The thermally induced phase separation behavior of the PES solutions is exemplified by the photographs shown in Figure 1a and S1 (Supporting Information). The dissolution test validated the trend suggested by the RED values, as depicted in Figure 1b. The solvents with RED ≥ 1.2 failed to completely dissolve PES even at a high temperature, whereas those with RED < 1.0 dissolved PES. The marginal solvents with 1.0 ≤ RED < 1.2 led to complete or partial dissolution. In this range, it was found that the dissolution behavior is affected by another molecular parameter of the solvent, the molar volume (V_m), which represents the size of a solvent molecule. Four solvents with $V_m \leq 128$ cm^3/mol enabled complete dissolution at high temperatures, whereas EGMBE and ethyl cinnamate with $V_m \geq 143$ cm^3/mol, only partially dissolved the PES. The incomplete dissolution gave an opaque solution or a rubbery paste with a transparent supernatant, implying that it was not the result of the slow permeation kinetics of large solvents into the free volume of glassy PES, but insufficient thermodynamic free energy for molecular mixing.

PES solutions that were completely dissolved at high temperatures were cooled to room temperature under vigorous stirring. The turbidity of the solutions was classified into two, as shown in Figure 2c. Solvents, such as NMP and DMSO with $\delta_P \geq 11.4$, and $\delta_H \geq 7.2$ maintained PES dissolution at room temperature for more than a week. The solvents, such as NB and DMB with $\delta_P \leq 5.8$ or $\delta_H \leq 5.2$ exhibited an opaque appearance except for γ-butyrolactone. The opaque appearance was ascribed to the phase separation in the solution. Hereafter, this study focused on the NB solvent because it was interesting that the NB caused solvent-induced crystallization of

PES, forming spherical mesoporous microparticles spontaneously. Detailed studies of other solvent systems will be reported in a future paper.

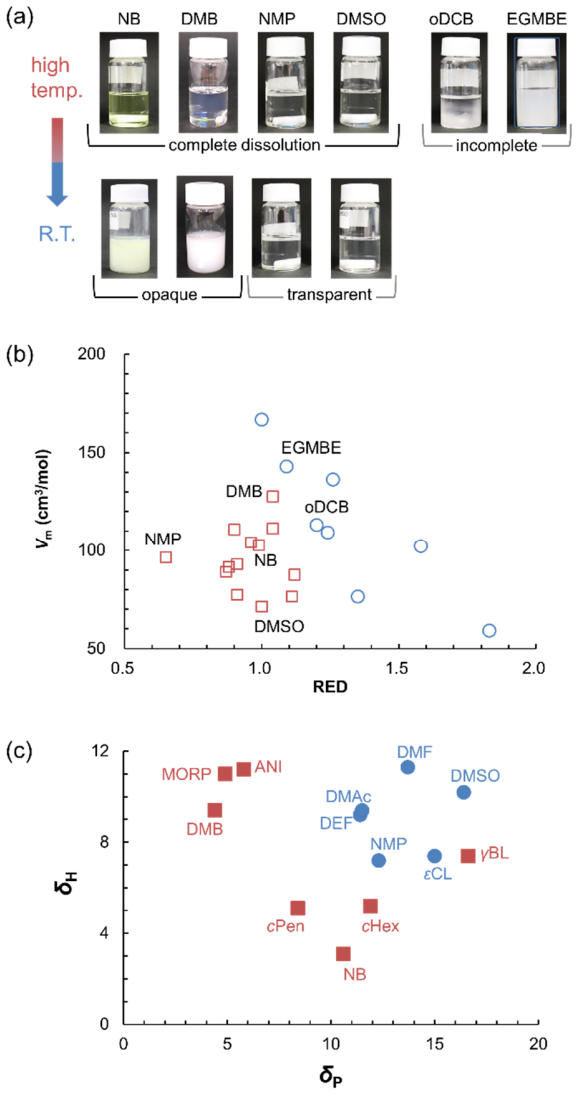

Figure 1. (a) Photographs of PES solutions in different organic solvents at a high temperature (upper) and at room temperature (lower). (b) Dissolution behavior of PES in organic solvents at high temperatures displayed as the plot between RED and V_m: complete dissolution (squares), incomplete dissolution (circles). The behaviors are summarized in Table S2 (Supporting

Information). (c) The turbidity of PES solutions at room temperature was classified into two on the plot of δ_P and δ_H: transparent (circles) or opaque (squares).

Crystallization kinetics

To follow the kinetics of phase separation in NB, the optical transmittance of solutions was monitored over time at a constant holding temperature (Figure 2a). When a 5-wt.% PES solution was kept at 20 °C, the change in transmittance started after 60 min and quickly decreased by 110 min. At 50 °C, the change in transmittance occurred after 220 min and gradually proceeded up to 450 min. The characteristic time of phase separation was defined as the time at 50% transmittance (Figure 2b). The kinetics became quicker at a lower temperature owing to the higher supersaturation of the PES solutions. When the PES concentration was increased to 20 wt.%, the transmittance change accelerated considerably (Figure 2b). The 20-wt.% solution had an opaque appearance after approximately 20 min. The acceleration at high concentration was also due to high supersaturation, which is consistent with the temperature dependence and common behavior of polymer crystallization in a solution [38]. Upon heating, the transmittance of the opaque solutions recovered steeply at high temperatures (Figure 2c). The solutions showed reversible temperature changes, indicating the reversible formation of polymer aggregates from the isolated polymers in the dissolution state. These aggregates were determined to be PES crystals, as discussed later. The maximum temperature of the opaque appearance characterizes the thermal stability of the PES crystals in the solution state. The 20-wt.% solution showed an upper temperature of 94 °C, whereas that for the 5-wt.% solution was reduced to 85 °C due to lower supersaturation.

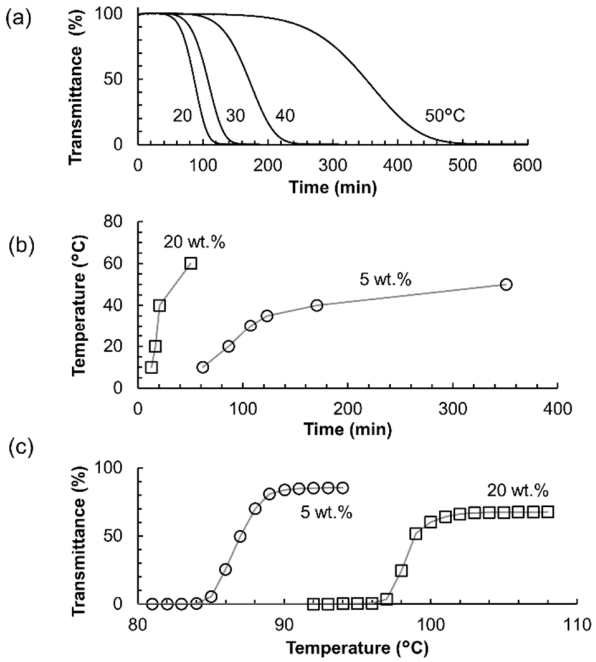

Figure 2. (a) Optical transmittance of the 5-wt.% PES solution monitored with time at several holding temperatures. (b) Characteristic times of transmittance change determined at various holding temperatures. (c) Reversible change in transmittance recorded by heating at high temperatures. Circle and square symbols represent 5-wt.% and 20-wt.% solutions, respectively.

Mesoporosity of PES microparticles

PES microparticles were readily collected from white solutions in high yields with slight handling loss. The P20 microparticles were nearly spherical with a diameter range of 2–6 μm (Figure 3a). The size distribution of P20 in the dispersed state was characterized by the laser diffraction method. The particle size distribution exhibited a large peak and a small peak at 7.5 μm and 1 μm, respectively (Figure 3b). The average diameter (D_{av}), the median (D_{med}), and D_{90} were determined to be 4.9 μm, 5.8 μm, and 9.8 μm, respectively. The D_{av} was consistent with the particle sizes observed in the SEM images. The D_{med} coincident with D_{av} and small D_{90} approximately 2 times of D_{av} confirmed the small size distribution of P20. A surface SEM image

of P20 revealed the fibrillar network of PES and numerous mesopores smaller than 100 nm (Figure 3c). These mesopores could be quantitatively characterized by nitrogen gas adsorption analysis. The adsorption/desorption isotherm of P20 showed Type II isotherm with a Type H3 hysteresis loop (Figure 3d), which suggests that the pore network had macropores that were not completely filled with pore condensation [39]. P20 had large total pore volume (V_{total}) of 0.59 cm^3/g, mesopore volume (V_{meso}) of 0.48 cm^3/g, and a specific surface area (S_{BET}) of 205 m^2/g. Ignoring the macropores that are undetectable by nitrogen gas adsorption, the porosity of a microparticle ϕ can be expressed by the relation: $\phi = V_{total} / (V_{total} + 1/\rho)$, where ρ is the true density of the polymer. Using a PES density of 1.37 g/cm^3 and V_{total} of 0.59 cm^3/g, ϕ was calculated to be 0.44. The pore size distribution exhibited a sharp peak at 7 nm (Figure 3e), which confirmed the mesoporous structure of the PES microparticles.

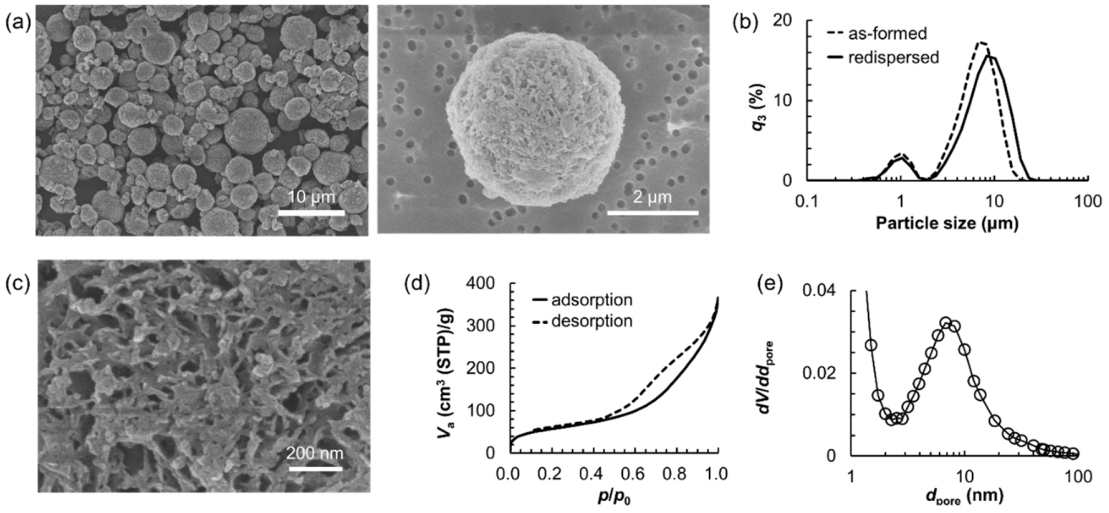

Figure 3. (a) SEM images of P20 microparticles. (b) Particle size distribution of as-formed P20 in solution (dashed line) and redispersed P20 after drying (solid line). (c) Surface morphology of P20 microparticles. (d) Nitrogen adsorption/desorption isotherm of P20 at −196 °C. (e) Pore size distribution of P20 analyzed by nitrogen adsorption analysis.

Crystalline structure of PES microparticles

The PES microparticles were characterized using XRD in both wet and dried states. While pristine PES exhibited only a broad halo due to the amorphous structure, the wet microparticles exhibited several distinct XRD peaks in the 2θ range of 5–35 °, indicating a crystalline structure (Figure 4). The XRD pattern of the dried microparticles also exhibited four strong peaks and eight weak peaks at the same 2θ values. Strong peaks were observed at 13.4°, 16.8°, 17.9°, and 24.4°, which correspond to *d* spacings of 6.60 Å, 5.27 Å, 4.96 Å, and 3.65 Å, respectively. Specific values of the XRD peaks are summarized in Table S3 (Supporting Information). Compared to the wet microparticles, the dried ones showed a relatively flat baseline, implying less amorphous regions. This indicates that the crystalline structure formed in the solution was preserved during the purification processes, including methanol washing and vacuum drying at room temperature. Some peaks marked by circular symbols showed similar peak intensities between the wet and dried microparticles, while the others marked by cross symbols decreased the intensity of the dried microparticles. This result might indicate that the microparticles grown in NB contain a polymorph of the crystals.

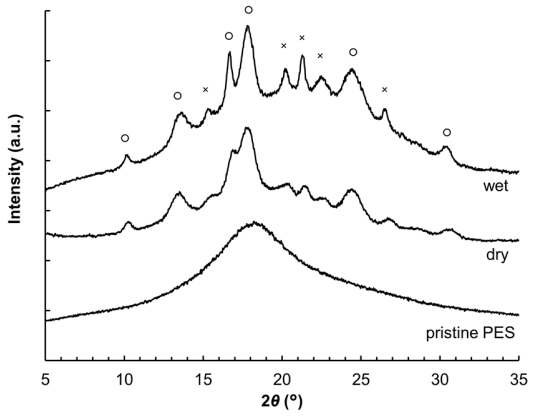

Figure 4. XRD pattern of pristine PES and P20 in wet and dried states.

Cocrystals of PES and NB molecules

To confirm the entrapped NB molecules in the microparticles, the FT-IR spectrum of P20 was compared with those of pristine PES powder and NB solvent (Figure 5a). The FT-IR spectrum of P20 showed sharp peaks at the same wavenumbers as the pristine PES. In addition, small but distinct peaks were observed at 1346 cm^{-1} and 1521 cm^{-1} due to the presence of NB. The peak series of P20 attributed to PES or NB confirmed that P20 contained NB. The entrapment of NB molecules was further confirmed by Raman spectroscopy (Figure 5b), where in addition to the characteristic Raman peaks of PES, P20 exhibited sharp peaks at 1001 cm^{-1} and 1343 cm^{-1}, which were attributed to NB.

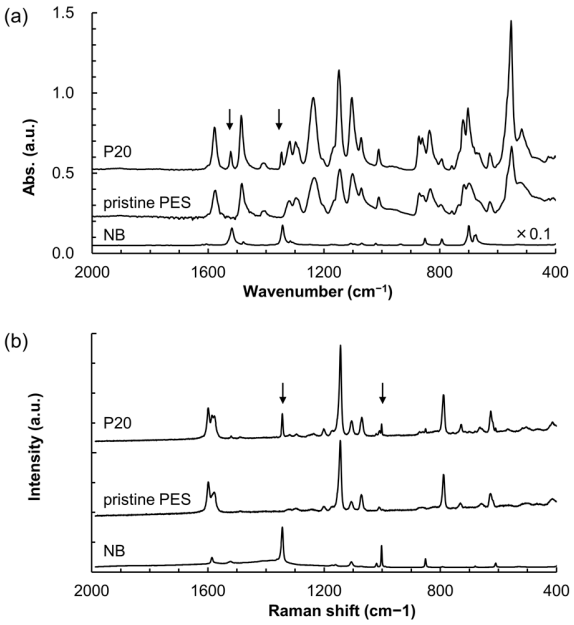

Figure 5. (a) FT-IR and (b) Raman spectra of P20, pristine PES, and NB solvent. The arrows indicate the peaks originating from entrapped NB molecules.

The presence of NB molecules in P20 was further confirmed via TGA (Figure 6a). P20 exhibited a 10% reduction in sample mass during the heating process up to 300 °C. The mass reduction started at the onset temperature of 146.8 °C and ended at 210 °C. The onset and endset temperatures are consistent with the T_m of P20 and the T_b of NB (210.9 °C). Considering the negligible mass change of PES, the mass reduction was attributed to the loss of NB molecules.

When P20 was heated to 300 °C in the DSC experiment, the first heating curve exhibited a blurry baseline shift in the 89–109°C and a sharp endothermic peak with an onset temperature of 153.6°C and an enthalpy of 11.1 J/g (Figure 6b, Figure S1). The baseline shift represents T_g, which is much lower than that of pristine PES due to the plasticization effect of NB molecule. The peak appeared above T_g indicates the melting of the cocrystals. After the second cycle, no peak was observed due to the dissociation of NB molecules from the cocrystal. In fact, GPC analyzed the molecular weights of PES in P20 (M_n: 28100, M_w: 47500) and those after DSC (M_n: 28500, M_w: 47000), which are almost the same with the pristine PES. Preparing microparticles and DSC analysis of the microparticles does not change the molecular weight of PES, indicating no chemical reaction and thermal degradation in the fabrication process and the characterization. In contrast to the heating process, no exothermic peak was observed during the cooling process (from 20 to −60 °C) (Figure S2). This suggests that the NB molecules did not behave as a crystallizable free solvent because they were trapped in the molecular-sized space of the PES crystal and/or strongly interacted with the polymer chains.

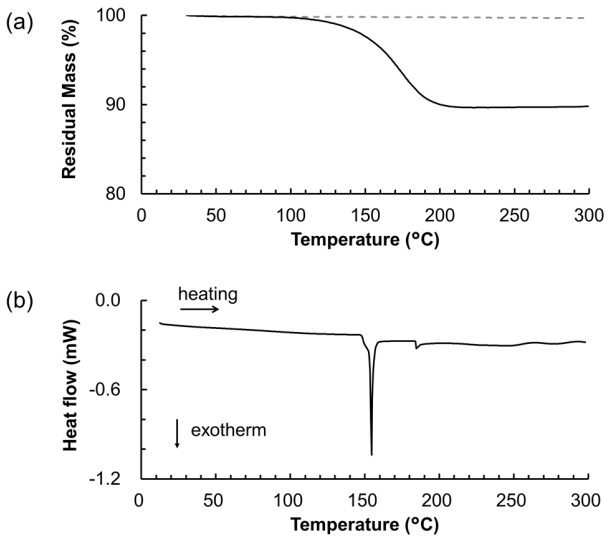

Figure 6. (a) DSC curve and (b) TGA profile of P20. The dashed line represents the TGA profile of pristine PES. To prevent the loss of NB molecules before data acquisition, unheated microparticles were used and the DSC and TGA curves were recorded at the first run.

Effect of PES concentration

The polymer concentration generally affects the thermally induced gelation of solutions driven by polymer crystallization [35]. When PES crystallization occurred at room temperature, PES concentrations up to 20 wt.% produced a white slurry that maintained its fluidity for at least a few weeks. This is interesting because thermally induced gelation may occur even at a low polymer concentration (≤10 wt.%) [35,40–43]. The fluidity of the PES solutions was attributed to the crystalline particles isolated from each other, well contrasted with nanofibrillar network in physical gels. When the concentration was increased to 40 wt.%, the solutions finally solidified. Compared to a soft sticky gel generally obtained via thermo-reversible gelation of a polymer solution, the solid was relatively hard but fragile and could be readily crushed into small pieces

by a spatula. When the pieces were ground by magnetic stirring in the dilution with NB, a slurry was obtained and microparticles were collected by washing and vacuum-drying.

The particle morphology of the PES crystals showed a concentration dependence (Figure 7). In contrast to the spherical shape of P20 (Figure 3(a-c)), P5 had curved discs or twisted dumbbell shapes (Figure 7a). P10 showed a folded or branched platelet structure (Figure 7b). The shapes of P5 and P10 appeared to be mid-spherical, which probably resulted from a shortage of PES polymer because many crystal nuclei are generated under vigorous stirring at room temperature. By contrast, P40 showed nearly spherical microparticles, similar to P20 (Figure 7c).

The particle size distribution determined via laser diffraction exhibited a slight dependence on the polymer concentration (Figure 7d). P40 had a D_{av} of 6.0 μm, which is slightly larger than that of P20 because P40 grew in a solid phase involving a partial fusion of microparticles. P5 and P10 exhibited larger D_{av} because of many unfolded polymer chains on crystal growth fronts, which quickly aggregated on contacting poor solvent (methanol) during the washing process. Despite the aggregation, P5 and P10 exhibited quite a narrow size distribution, as confirmed by the coinciding D_{av} and D_{med} and a small D_{90}. It is noteworthy that such spherical microparticles were never obtained via mechanical crushing or ultrasonication of a soft sticky gel consisting of a percolated network of polymer crystals.

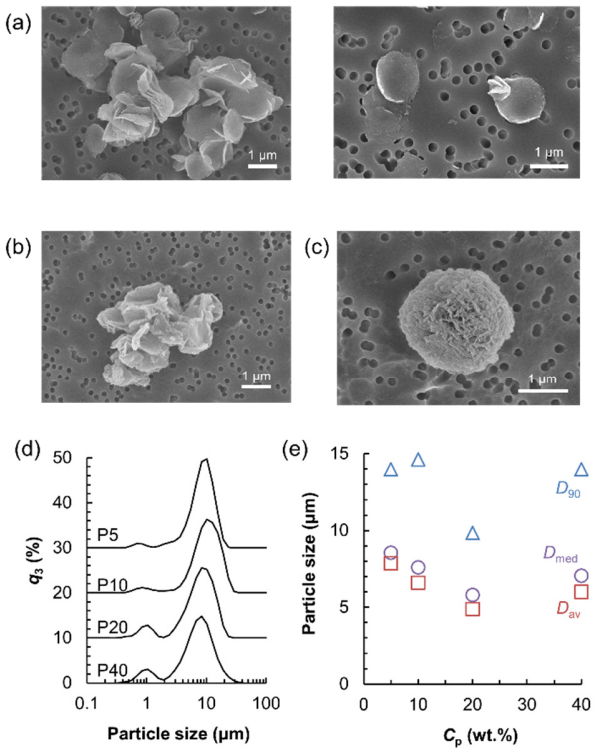

Figure 7. SEM images of mesoporous (a) P5, (b) P10, and (c) P40 microparticles. (d) Particle size distributions of P5, P10, P20, and P20. (e) Statistical parameters of microparticle size (D_{av}, D_{med}, and D_{90}) plotted as a function of C_p.

In contrast to the concentration-dependent morphology, the PES microparticles exhibited identical XRD patterns, indicating that the microparticles had the same microstructure irrespective of the concentration (Figure 8). Furthermore, DSC for P5, P10, and P40 showed a sharp exothermic peak with a onset temperature at 157°C and an enthalpy of 15–17 J/g (Figure S3), which is consistent with P20 and supports the crystallinity of the microparticles independent on PES concentration. Therefore, the different morphologies of the microparticles could be attributed to the different growth pathways consisting of the same crystalline components. At higher concentrations, all XRD peaks became prominent and sharp, suggesting several

possibilities, such as an increased crystallinity, an increase in crystal size, and/or reduced crystalline disorder and defects.

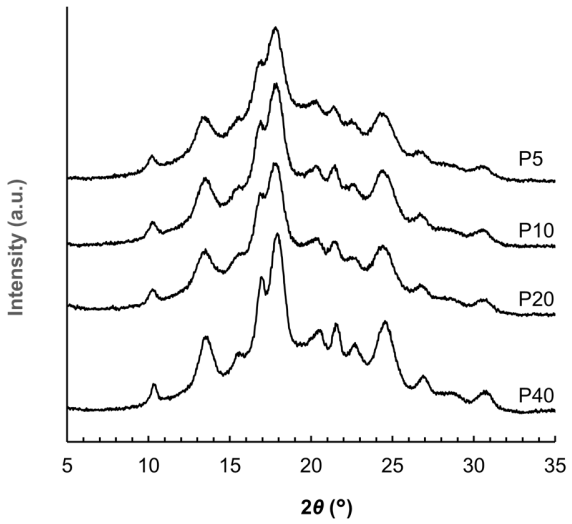

Figure 8. XRD patterns of P5, P10, P20, and P40 microparticles in dried state.

All microparticles exhibited mesoporosity that was detectable by nitrogen gas adsorption (Figure 9a). The particles with spherical shapes, P20 and P40, had a single peak at 7 nm, whereas P5 and P10 showed broader pore size distribution with an additional peak at 5 nm (Figure 9b). P40 had an S_{BET} of 170 m^2/g and V_{meso} of 0.40 cm^3/g, which were slightly larger than those of P5 and P10 (Figure 9c). Despite widely different morphologies, all microparticles showed similar mesoporosity with slight variations in S_{BET}, pore size, and volume. This suggests an interesting possibility where the microstructure of the PES crystal primarily influences the mesoporosity, because both the XRD patterns and mesoporosity showed little dependence on the polymer concentration.

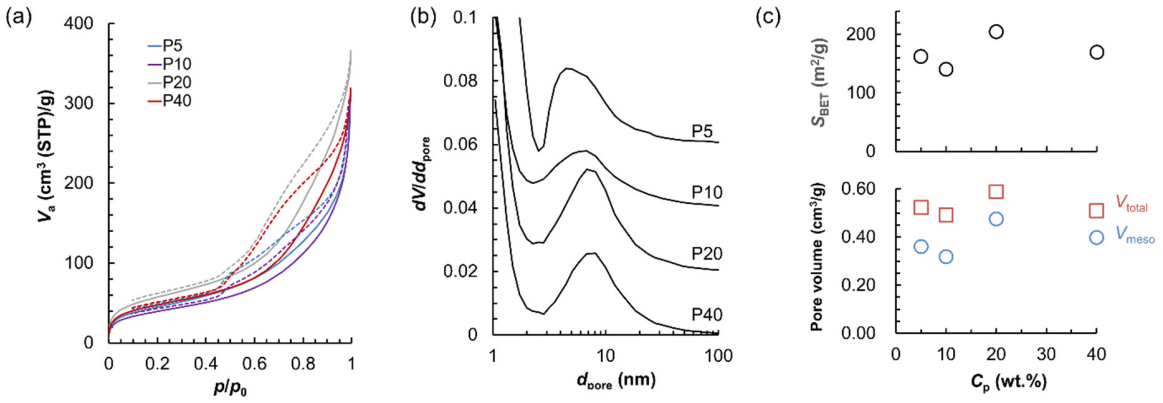

Figure 9. (a) Nitrogen adsorption isotherm of PES microparticles at −196 °C (solid: adsorption; dashed: desorption). (b) Pore size distribution of PES microparticles. (c) S_{BET} and pore volumes (V_{total}, V_{meso}) of the microparticles plotted as a function of C_p.

Tracking the growth process of PES microparticles

To investigate the formation process of the PES microparticles, aliquots of the 20-wt.% solution were taken at several crystallization periods and microparticles were collected via methanol precipitation. The PES solution was transparent up to 0.5 h and gradually became turbid after 1.0 h (Figure 10a). When transparent solutions were injected into excess methanol, the resulting dispersions had a white supernatant and large precipitates at the bottom. The particle size distribution of the dispersion exhibited a large peak at 20–40 μm and a small peak at 120 μm (Figure 10b). SEM images showed irregular flakes larger than tens of micrometers and numerous nanoparticles (Figure 10c). No spherical mesoporous microparticles were present, as observed previously (Figure 3b). As confirmed by the 0-h solution, a mixture of large flakes and numerous nanoparticles are usually obtained when a polymer solution completely dissolves and is injected into an excess of poor solvent. The dispersion obtained from the 1-h solution had detectable numbers of textured microparticles with a size of approximately 1 μm, as well as many

nanoparticles (Figure 10c). The textured microparticles had similar morphologies observed for low concentration solutions, as shown in Figure 7a, which could be considered as an intermediate of a spherical spherulite. After 1.5 h, the particle size distribution decreased with time because of the suppression of irregular large flakes during the recovery process (Figure 10b). Microparticles collected from the 1.5-h solution had a mesoporous structure similar to that of P20 (Figure 10c). The S_{BET} and pore volumes slightly increased after 24 h of crystallization and were saturated after prolonged crystallization up to 48 h (Figure 10d).

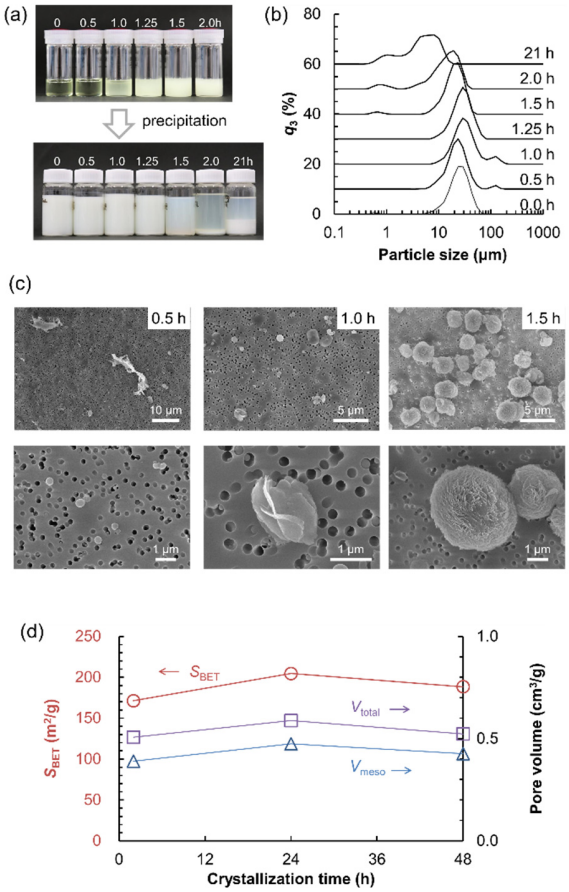

Figure 10. (a) Photographs of PES solutions (upper) and PES particles precipitated in methanol (lower). (b) Particle size distribution of the dispersions. (c) SEM images of PES microparticles. (d) Specific surface area and pore volumes of PES particles.

Formation mechanism of PES microparticles

Recently, Crist et al. reviewed the structure and formation mechanism of polymer spherulites [44]. A spherulite is a polycrystalline morphology formed by the assembly of microcrystals, which is frequently observed during the crystallization of polymers in viscous melt and solutions at deep supercooling. The deep supercooling of the solutions agrees with the process conditions of this experiment. The primary component of polymer spherulite is a lamellar structure composed of folded polymer chains. Branch formation during lamellar growth is the key for determining the macroscopic morphology of spherulites [45,46]. Gránásy et al. reproduced various morphologies of spherulites using a phase-field simulation in a two-dimensional model by considering crystal grain nucleation at the growth front (growth front nucleation) [47]. Random branching of lamellae makes crystal growth isotropic and results in spherical crystal morphology, which occurs at deep supercooling owing to the reduction of the rotational to translational diffusion coefficient ratio. In this study, platelet and sheaf-like intermediates, as well as partially opened spheres, were found during the growth process. The morphologies suggest that the formation mechanism of PES microparticles corresponds to the well-known sheaf-like unidirectional growth model of spherical polymer spherulite proposed in the previous study [45].

High nucleation rate of isolated crystal nuclei and slow growth of the nuclei favor the growth of small crystalline microparticles because the conditions promote the simultaneous crystal growth of large numbers of crystal nuclei. By contrast, the formation of uniformly sized crystalline microparticles requires no additional nucleation during the crystal growth. This condition is satisfied by crystal growth that is sufficiently faster than crystal nucleation. Thus, the small size and size uniformity of crystalline microparticles require conflicting conditions on the nucleation and growth rate, which are normally difficult to achieve under solution crystallization without

external stimuli. In this study, the solution was vigorously stirred during the cooling and crystallization processes, which facilitates the formation of microparticles. In fact, the 20-wt.% solution kept at room temperature without stirring was transparent for more than a week, and countable crystal nuclei appeared only on the vial wall and grew to a large size (Figure S4). A possible route for microparticle formation is shown in Figure 11, on which small crystalline intermediates that spontaneously form in the initial stage of polymer spherulite are mechanically pulverized and results in numerous seeds for crystalline microparticles. There remains a challenge to completely reveal the entire mechanism of the formation of highly ordered structures via solvent-induced crystallization. The initial stage of the microparticle formation is currently being investigated and will be reported.

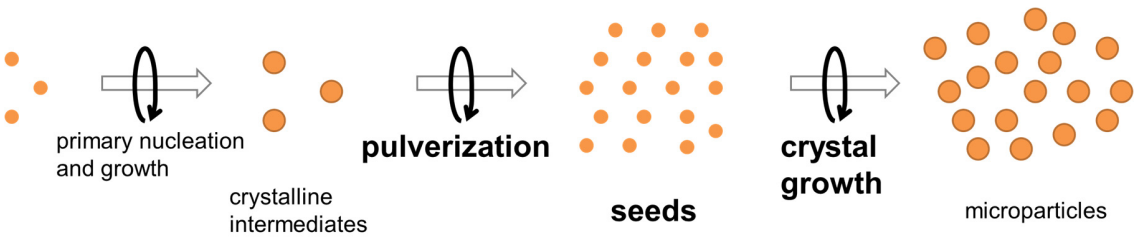

Figure 11. Schematic illustration of the formation mechanism of microparticles

CONCLUSION

Thermally induced phase separation of PES was investigated using 21 organic solvents. Based on HSP, the behaviors were categorized into three categories: incomplete dissolution at a high temperature, prolonged dissolution at room temperature, and phase separation upon cooling to room temperature. The solvent, NB caused the crystallization of PES, forming cocrystals of PES

and NB. The crystalline structure and thermal properties of the cocrystals were characterized using XRD and DSC. The entrapped NB solvents were confirmed by FT-IR, Raman spectroscopy, and thermogravimetric analysis (TGA). The cocrystals were stable under vacuum drying at room temperature. The NB-induced crystallization resulted in nearly spherical microparticles with a diameter of 6 μm. The microparticle had a mesoporous morphology with a porosity of 0.44, and pore size distribution peaking at 7 nm. Based on the concentration dependence of microparticle formation and tracking of the crystal growth process, the mechanism of microparticle formation was elucidated by the theory of polymer spherulites.

The phenomenon of solvent-induced crystallization is still not very well understood and the crystallization behavior of rigid high-T_g polymers is intriguing in polymer science. A detailed study on the formation process of the microparticle, particularly in the initial stage, will provide concrete understanding and open a way to design high-ordered structure of homopolymers using solution crystallization. In contrast to the mesoporosity of PES-NB cocrystals demonstrated in this study, a nanoporous structure of PES may be obtained if NB molecules can be extracted without loss of crystallinity, as was successfully achieved in a nanoporous morphology of syndiotactic polystyrene and poly(2,6-dimethyl-1,4-phenylene oxide) via supercritical carbon dioxide drying [22,48]. As there are several practical applications of mesoporous particles, this process is very much relevant for research on colloids, adsorption, catalysis, drug delivery, and environmental and energy-related materials.

ASSOCIATED CONTENT

Supporting Information: Tabulated properties of all the organic solvents used in this study, dissolution and turbidity parameters for PES solutions, XRD peaks values and d-spacings for Figure 4 and Figure 8, and photograph of 20-wt.% PES solution.

AUTHOR INFORMATION

*Corresponding Author

Sadaki Samitsu

National Institute for Materials Science (NIMS), 1-2-1, Sengen, Tsukuba, Ibaraki 305-0047, Japan

ACKNOWLEDGMENT

Author thanks Dr. Takashi Hiroi for the informative discussion on polymer crystallization in solution. I appreciate Prof. Izumi Ichinose, Prof. Masanobu Naito, Dr. Yasuyuki Nakamura, Prof. Masayuki Takeuchi, and Dr. Atsuro Takai for instrumental support with SEM, transmittance measurements, GPC, and TGA, respectively. The author acknowledges Dr. Yoshitaka Matsushita and Dr. Takanobu Hiroto for the XRD measurements. I thank Ms. Aya Hiyama and Ms. Miwa Ohniwa for their support in conducting the preliminary exploration of particle fabrication and particle size analysis. Particle size analysis, FT-IR, and Raman spectroscopy were performed under instrumental support by the NIMS Molecule & Material Synthesis Platform as part of the Nanotechnology Platform of the Ministry of Education, Culture, Sports, Science and Technology (MEXT), Japan. S.S. acknowledges the financial support provided by JSPS KAKENHI (Grant Nos.: JP17K06007 and 21H02006).

References

(1) Zhang, W.; Zhao, Q.; Yuan, J. Porous Polyelectrolytes: The Interplay of Charge and Pores for New Functionalities. *Angew. Chemie Int. Ed.* **2018**, *57* (23), 6754–6773.

(2) Bhanja, P.; Palui, A.; Chatterjee, S.; Kaneti, Y. V.; Na, J.; Sugahara, Y.; Bhaumik, A.; Yamauchi, Y. Crystalline Porous Organic Polymer Bearing −SO 3 H Functionality for High Proton Conductivity. *ACS Sustain. Chem. Eng.* **2020**, *8* (6), 2423–2432.

(3) Fan, J. B.; Huang, C.; Jiang, L.; Wang, S. Nanoporous Microspheres: From Controllable Synthesis to Healthcare Applications. *J. Mater. Chem. B* **2013**, *1* (17), 2222–2235.

(4) Zhou, M.; Shen, L.; Lin, X.; Hong, Y.; Feng, Y. Design and Pharmaceutical Applications of Porous Particles. *RSC Adv.* **2017**, *7* (63), 39490–39501.

(5) Sun, Q.; Dai, Z.; Meng, X.; Xiao, F. S. Porous Polymer Catalysts with Hierarchical Structures. *Chem. Soc. Rev.* **2015**, *44* (17), 6018–6034.

(6) Liu, F.; Kong, W.; Qi, C.; Zhu, L.; Xiao, F.-S. Design and Synthesis of Mesoporous Polymer-Based Solid Acid Catalysts with Excellent Hydrophobicity and Extraordinary Catalytic Activity. *ACS Catal.* **2012**, *2* (4), 565–572.

(7) Samitsu, S.; Miyazaki, H. T.; Segawa, H. Transmitting and Scattering Colors of Porous Particles of Poly(Vinyl Chloride) Based on Christiansen Effect. *Polymer* **2018**, *147*, 237–246.

(8) Wang, B.; Prinsen, P.; Wang, H.; Bai, Z.; Wang, H.; Luque, R.; Xuan, J. Macroporous Materials: Microfluidic Fabrication, Functionalization and Applications. *Chem. Soc. Rev.* **2017**, *46* (3), 855–914.

(9) Wintzheimer, S.; Granath, T.; Oppmann, M.; Kister, T.; Thai, T.; Kraus, T.; Vogel, N.; Mandel, K. Supraparticles: Functionality from Uniform Structural Motifs. *ACS Nano* **2018**, *12* (6), 5093–5120.

(10) Kasai, H.; Mitsui, H.; Zhao, G.; Ishizaka, T.; Suzuki, M.; Oikawa, H.; Nakanishi, H. Fabrication of Porous Nanoscale Polyimide Structures. *Chem. Lett.* **2008**, *37* (10), 1056–1057.

(11) Gokmen, M. T.; Du Prez, F. E. Porous Polymer Particles—A Comprehensive Guide to Synthesis, Characterization, Functionalization and Applications. *Prog. Polym. Sci.* **2012**, *37* (3), 365–405.

(12) Okay, O. Macroporous Copolymer Networks. *Prog. Polym. Sci.* **2000**, *25* (6), 711–779.

(13) Weber, J.; Bergström, L. Impact of Cross-Linking Density and Glassy Chain Dynamics on Pore Stability in Mesoporous Poly(Styrene). *Macromolecules* **2009**, *42* (21), 8234–8240.

(14) Lloyd, D. R.; Kinzer, K. E.; Tseng, H. S. Microporous Membrane Formation via Thermally Induced Phase Separation. I. Solid-Liquid Phase Separation. *J. Membr. Sci.* **1990**, *52* (3), 239–261.

(15) Van De Witte, P.; Dijkstra, P. J.; Van Den Berg, J. W. A.; Feijen, J. Phase Separation Processes in Polymer Solutions in Relation to Membrane Formation. *J. Membr. Sci.* **1996**, *117* (1–2), 1–31.

(16) Sasaki, T.; Yamamoto, Y.; Takahashi, T. Spherulitic Growth of Poly(Ethylene Oxide) from Viscous Solution. *Polym. J.* **1998**, *30* (11), 868–873.

(17) Sasaki, T.; Miyazaki, A.; Sugiura, S.; Okada, K. Crystallization of Poly(Ethylene Oxide) from Solutions of Different Solvents. *Polym. J.* **2002**, *34* (11), 794–800.

(18) Sasaki, T.; Kurita, M.; Yabu, T.; Takahashi, T. Diffusion Aspects in the Crystallization of Isotactic Polystyrene from Solutions. *Macromolecules* **1995**, *28* (25), 8528–8534.

(19) Sasaki, T.; Asakawa, R.; Sakurai, K. Formation of Porous Spherulites of Poly(L-Lactide) Grown from Solutions. *Polym. J.* **2009**, *41* (9), 787–791.

(20) Asano, Y.; Nakayama, K.; Yao, S. Creation of Functional Materials by Use of a Slow Crystallization Process in the Nonequilibrium State. I. Porous Polyamide Microparticles. *J. Appl. Polym. Sci.* **2003**, *90* (9), 2428–2432.

(21) Rahman, M. A.; Renna, L. A.; Venkataraman, D.; Desbois, P.; Lesser, A. J. High Crystalline, Porous Polyamide 6 by Anionic Polymerization. *Polymer* **2018**, *138*, 8–16.

(22) Reverchon, E.; Guerra, G.; Venditto, V. Regeneration of Nanoporous Crystalline Syndiotactic Polystyrene by Supercritical CO2. *J. Appl. Polym. Sci.* **1999**, *74* (8), 2077–2082.

(23) Nagendra, B.; Cozzolino, A.; Daniel, C.; Rizzo, P.; Guerra, G.; Auriemma, F.; De Rosa, C.; D'Alterio, M. C.; Tarallo, O.; Nuzzo, A. Two Nanoporous Crystalline Forms of Poly(2,6-Dimethyl-1,4-Phenylene)Oxide and Related Co-Crystalline Forms. *Macromolecules* **2019**, *52* (24), 9646–9656.

(24) Sheldon, R. P.; Blakey, P. R. Liquid-Induced Crystallization in Polymers. *Nature* **1962**, *195* (4837), 172–173.

(25) Vittoria, V.; Riva, F. Solvent-Induced Crystallization of Quenched Isotactic Polypropylene in Different Liquids. *Macromolecules* **1986**, *19* (7), 1975–1979.

(26) Tashiro, K.; Ueno, Y.; Yoshioka, A.; Kobayashi, M. Molecular Mechanism of Solvent-Induced Crystallization of Syndiotactic Polystyrene Glass. 1. Time-Resolved Measurements of Infrared/Raman Spectra and X-Ray Diffraction. *Macromolecules* **2001**, *34* (2), 310–315.

(27) Tashiro, K.; Yoshioka, A. Molecular Mechanism of Solvent-Induced Crystallization of Syndiotactic Polystyrene Glass. 2. Detection of Enhanced Motion of the Amorphous Chains in the Induction Period of Crystallization. *Macromolecules* **2002**, *35* (2), 410–414.

(28) van Emmerik, P. T.; Smolders, C. A. Phase Separation in Polymer Solutions. II. Determination of Thermodynamic Parameters of Poly (2,6-Dimethyl-1,4-Phenylene Oxide) Toluene Mixtures. *J. Polym. Sci. Part C Polym. Symp.* **2007**, *39* (1), 311–324.

(29) Sato, S.; Gondo, D.; Wada, T.; Kanehashi, S.; Nagai, K. Effects of Various Liquid Organic Solvents on Solvent-Induced Crystallization of Amorphous Poly(Lactic Acid) Film. *J. Appl. Polym. Sci.* **2013**, *129* (3), 1607–1617.

(30) Guenet, J.-M. *Polymer-Solvent Molecular Compounds*; Elsevier, 2008.

(31) Blackadder, D. A.; Ghavamikia, H.; Windle, A. H. Evidence for Crystallinity in Poly(Ether Sulphone). *Polymer* **1979**, *20* (6), 781–782.

(32) Blackadder, D. A.; Ghavamikia, H. Crystallinity in Polyethersulphone: A Problem of Definition. *Polymer* **1979**, *20* (11), 1433–1434.

(33) Benhalima, A.; Hudon, F.; Koulibaly, F.; Tessier, C.; Brisson, J. Polyethersulfone Polymers and Oligomers — Morphology and Crystallization. *Can. J. Chem.* **2012**, *90* (10), 880–890.

(34) Grünig, L. E.; Meyer, A.; Emmler, T.; Abetz, V.; Handge, U. A. Solvent-Induced Crystallization of Poly(Phenylene Sulfone). *Macromolecules* **2021**, *54* (10), 4816–4826.

(35) Samitsu, S. Thermally Stable Mesoporous Poly(Ether Sulfone) Monoliths with Nanofiber Network Structures. *Macromolecules* **2018**, *51* (1), 151–160.

(36) Marcus, Y. *The Properties of Solvents*; Wiley, 1998.

(37) Hansen, C. M. *Hansen Solubility Parameters: A User's Handbook*; CRC Press, 2007.

(38) Mandelkern, L. *Crystallization of Polymers Volume 2: Kinetics and Mechanisms*; Cambridge University Press, 2004.

(39) Thommes, M.; Kaneko, K.; Neimark, A. V.; Olivier, J. P.; Rodriguez-Reinoso, F.; Rouquerol, J.; Sing, K. S. W. Physisorption of Gases, with Special Reference to the Evaluation of Surface Area and Pore Size Distribution (IUPAC Technical Report). *Pure Appl. Chem.* **2015**, *87* (9–10), 1051–1069.

(40) Tan, H. M.; Moet, A.; Hiltner, A.; Baer, E. Thermoreversible Gelation of Atactic Polystyrene Solutions. *Macromolecules* **1983**, *16* (1), 28–34.

(41) Guenet, J. M.; Mckenna, G. B. Thermoreversible Gelation of Isotactic Polystyrene: Thermodynamics and Phase Diagrams. *Macromolecules* **1988**, *21* (6), 1752–1756.

(42) Bashir, Z. Thermoreversible Gelation and Plasticization of Polyacrylonitrile. *Polymer* **1992**, *33* (20), 4304–4313.

(43) Berghams, H.; Donkers, A.; Frenay, L.; Stoks, W.; De Schryver, F. E.; Moldenaers, P.; Mewis, J. Thermoreversible Gelation of Syndiotactic Poly(Methyl Methacrylate). *Polymer* **1987**, *28* (1), 97–102.

(44) Crist, B.; Schultz, J. M. Polymer Spherulites: A Critical Review. *Prog. Polym. Sci.* **2016**, *56*, 1–63.

(45) Norton, D. R.; Keller, A. The Spherulitic and Lamellar Morphology of Melt-Crystallized Isotactic Polypropylene. *Polymer* **1985**, *26* (5), 704–716.

(46) Gránásy, L.; Pusztai, T.; Börzsönyi, T.; Warren, J. A.; Douglas, J. F. A General Mechanism of Polycrystalline Growth. *Nat. Mater.* **2004**, *3* (9), 645–650.

(47) Gránásy, L.; Pusztai, T.; Tegze, G.; Warren, J. A.; Douglas, J. F. Growth and Form of Spherulites. *Phys. Rev. E* **2005**, *72* (1), 011605.

(48) Daniel, C.; Longo, S.; Fasano, G.; Vitillo, J. G.; Guerra, G. Nanoporous Crystalline Phases of Poly(2,6-Dimethyl-1,4-Phenylene)Oxide. *Chem. Mater.* **2011**, *23* (13), 3195–3200.